Inherited textures during the perovskite to post-perovskite transition and seismic anisotropy in D''. Supplementary Information.

S1. Synthesis and transformation experiments

Starting single crystals of $NaNiF_3$ perovskite were grown in NaCl flux at 0.5 GPa at the ETH, Zurich. A stoichiometric mixture of NaF and NiF_2 was mixed in equal (weight) proportion with NaCl and ground under acetone. The dried fluoride-chloride mixture was then loaded into a 4.5 mm diameter gold capsule which was welded shut. This capsule was loaded into a 22 mm Talc/graphite piston cylinder assembly and compressed to 0.5 GPa. Once the cell was at pressure the temperature was increased to 1000 °C for 3 hours after which it was slowly reduced to 700 °C over a period of 11 days. The temperature was then quenched by cutting power to the furnace (over a period of ~10 minutes) and the sample slowly decompressed and recovered. The euhedral or subhedral transparent apple green ~1 mm crystals of $NaNiF_3$ perovskite, which were found by optical microscopy to be free of inclusions but occasionally twinned (Figure S1a, b), were recovered and cleaned by repeated rinsing in distilled water.

Three of these single crystals were loaded into a NaCl pressure medium inside a 1.2 mm diameter, 2.6 mm long, platinum capsule for the transformation experiment. Previous experience of partial transformation to post-perovskite of $NaMnF_3$ perovskite starting powder suggested that conditions of 22 GPa and 700 °C for 24 h would result in partial transformation of the $NaNiF_3$ single crystals to post-perovskite. This transformation experiment was performed using a 10 mm Cr-doped MgO octahedron compressed by 3.5 mm truncated tungsten carbide anvils in a Walker-type split-cylinder multi-anvil press at the ETH, Zurich. The furnace was LaCrO3 and there was no thermocouple in the cell; temperature was estimated from power-temperature relations in previous experiments. We estimate that the uncertainty in temperature at 700 °C is ± 50 °C. The experiment was terminated by cutting power to the furnace (over a period of ~5 minutes) followed by slow decompression (over a period of ~15 hours). The recovered samples were

cleaned by washing in distilled water and maintained their gross morphology. They were, however, cloudy in appearance and had rounded edges compared to the starting perovskite crystals (Figure S1c).

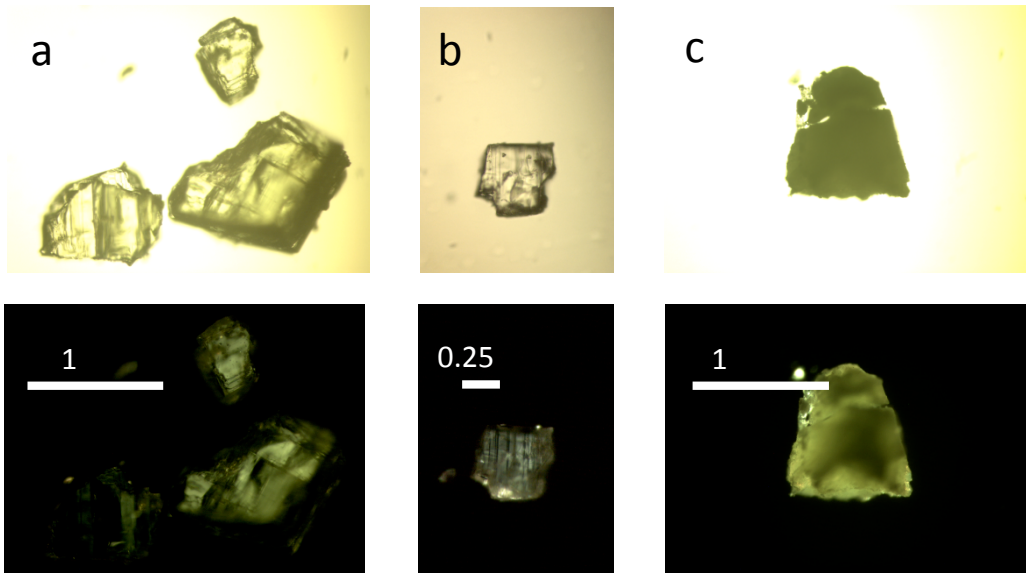

Figure S1. Optical micrographs of starting perovskite (a, b), and partially transformed to post-perovskite (c) $NaNiF_3$ single crystals. Upper panels are in plane-polarised light and lower panels under crossed polars. The starting perovskite is optically clean and smaller crystals occasionally show twinning (b); the twinning might be masked in the large crystals by their high birefringence and refraction effects from the surface morphology. The crystals recovered from the transformation experiment are cloudy in appearance and their birefringence does not show extinction, indicative of the polycrystalline nature of the recovered samples.

S2. X-ray diffraction experiments.

Single crystal data were collected at Diamond light source ltd. in the extreme conditions beamline (I15). The experiment was performed using a fully focused beam of λ = 0.20675 Å, as calibrated by diffraction from a NIST ruby sphere. A 20 µm circular pinhole defined the beam size and shape. Chips from partially transformed crystals of $NaNiF_3$, approximately 30 x 10 µm in size, were mounted with a MiTeGen micro loop on the diffractometer, data were then collected with an Atlas ccd detector (Agilent technologies)

scanning ϕ and ω with a width of 1°. The ϕ scan was performed in the range from -60° to +120° at a κ = -137.75°, ω = 56° while the ω scan was performed from 15 to 95° at ϕ = 98.00° and κ = -134.75°. Data were then treated within the Crysalis softare package to find the orientation matrices of the phases present in the sample.

Figure S2 shows the orientation of the *a*-axes of post-perovskite crystallites identified from the X-ray diffraction experiment projected onto the *a*-*b* plane of the host perovskite crystal, for the first sample studied. The other samples showed similar relations but the chips were too strained for good crystal indexing. The *c*-axes of the perovskite and post-perovskite are very close to coincidence (within about 1 degree) in all cases. Plotted in black, post-perovskite a-axes cluster around the perovskite b-axis, with a clear set of crystallites which are symmetrically distributed about the perovskite b-axis, at an angle of 33.5 degrees between the *a*-directions of the two post-perovskite orientations. As noted in the main text, this is the angular relationship expected for {110} twins in post-perovskite $NaNiF_3$. The dotted line is the expected angular relationship of post-perovskite *a*-axes if the martensitic transformation postulated in the main text is correct. Plotted in red are another set of post-perovskite *a*-axial directions which fall close to the perovskite *a*-direction. Once again, there is a set of post-perovskite a-axes which are separated by an angle of 33.5 degrees, however in this case they are not symmetrically distributed about the perovskite *a*-axis, but rather the mirror plane between them is at an angle of 8 degrees to the perovskite *a*-axis. This angle of 8 degrees is the angular divergence between sets of perovskite *a*- and *b*-axes if there is a {110} twinning relationship in the perovskite. While {110} perovskite twins were not observed in this sample they were observed in the other two samples studied. The red lines represent the predicted axial orientations of perovskite and post-perovskite produced from a (110) twin in the host perovskite. Of the ten post-perovskite crystallites identified in this diffraction experiment, 7 can be explained perfectly using the proposed Martensitic transformation mechanism. The other three have their *a*-axes close to the *a*-axis of the perovskite host crystal (or its twin) and possibly represent a similar transformation mechanism involving stacking faults in the perovskite *a*-direction. In this case, however, the octahedral tilts in the host perovskite break the mirror symmetry of the daughter post-perovskite and hence a further diffusive

rearrangement of some of the anions is required to construct the post-perovskite unit cell. Given that we observe over twice as many post-perovskite crystallites in the $\{110\}_{Ppv}$ll$(010)_{Pv}$ orientation by X-ray diffraction, and we only observe this orientation in the TEM study we suggest that the pure Martensitic transition involving stacking faults in the perovskite b-direction is the dominant mechanism. This is consistent with the stacking-fault energies calculated in Oganov et al., 1995.

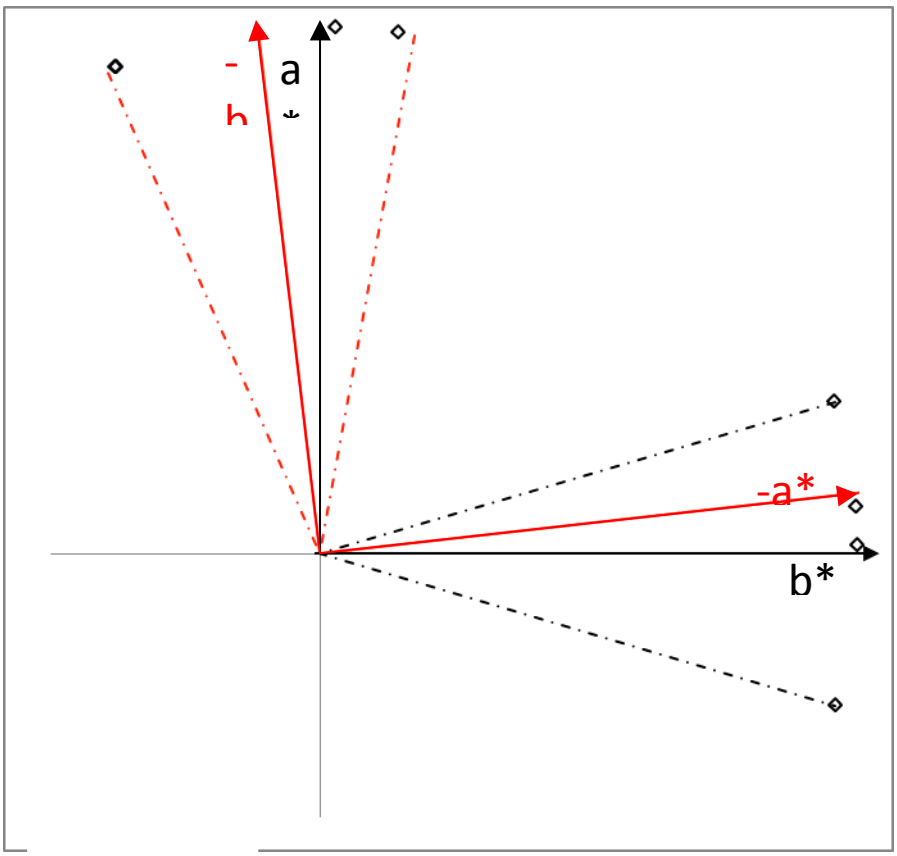

Figure S2. The orientation of the *a*-axes of post-perovskite crystallites within a perovskite (twinned) crystal identified from the X-ray diffraction experiment projected onto the *a*-*b* plane of the host perovskite crystal. The a and b reciprocal lattice vector directions of the perovskite twins are marked in bold and labelled: black for the perovskite used for the reference frame and red for its (110) twin.

S3. Transmission electron microscopy.

TEM characterizations were carried out at the Bayerisches Geoinstitut, Bayreuth, with a Philips *CM20FEG* equipped with an energy dispersive X-ray (EDX) analyzer, operated at 200 kV. A small chip from the sample used in the X-ray diffraction experiment was crushed under ethanol and the dispersion placed on a lacey carbon film on Cu-grid (200 mesh). The topotaxial relations between perovskite and post-perovskite and twin textures were investigated at first using conventional TEM techniques (selected area electron diffraction, bright-field and dark-field image, Figure. S3). In this TEM work, the convention of the orthorhombic symmetries (space group, ***Pbnm*** and ***Cmcm***) and the unit cell setting (c-axis > b-axis > a-axis and a-axis > c-axis > b-axis) are used for crystallographic directions, [u v w] or < u v w > and planes, (h k l) or {h k l} of the perovskite and post-perovskite, respectively. The detail of the $[001]_{Pv}$ oriented grain was further examined in the high-resolution lattice image (Figure 1). The chemistry of the grain was also cross-checked by using EDX spectroscopy. It was found that regions of perovskite-structured $NaNiF_3$ were stable to the electron beam but regions containing post-perovskite structured material slowly degraded by loss of sodium and fluorine. This beam-induced decomposition was, however, sufficiently slow for HR TEM images to be collected before significant damage had occurred.

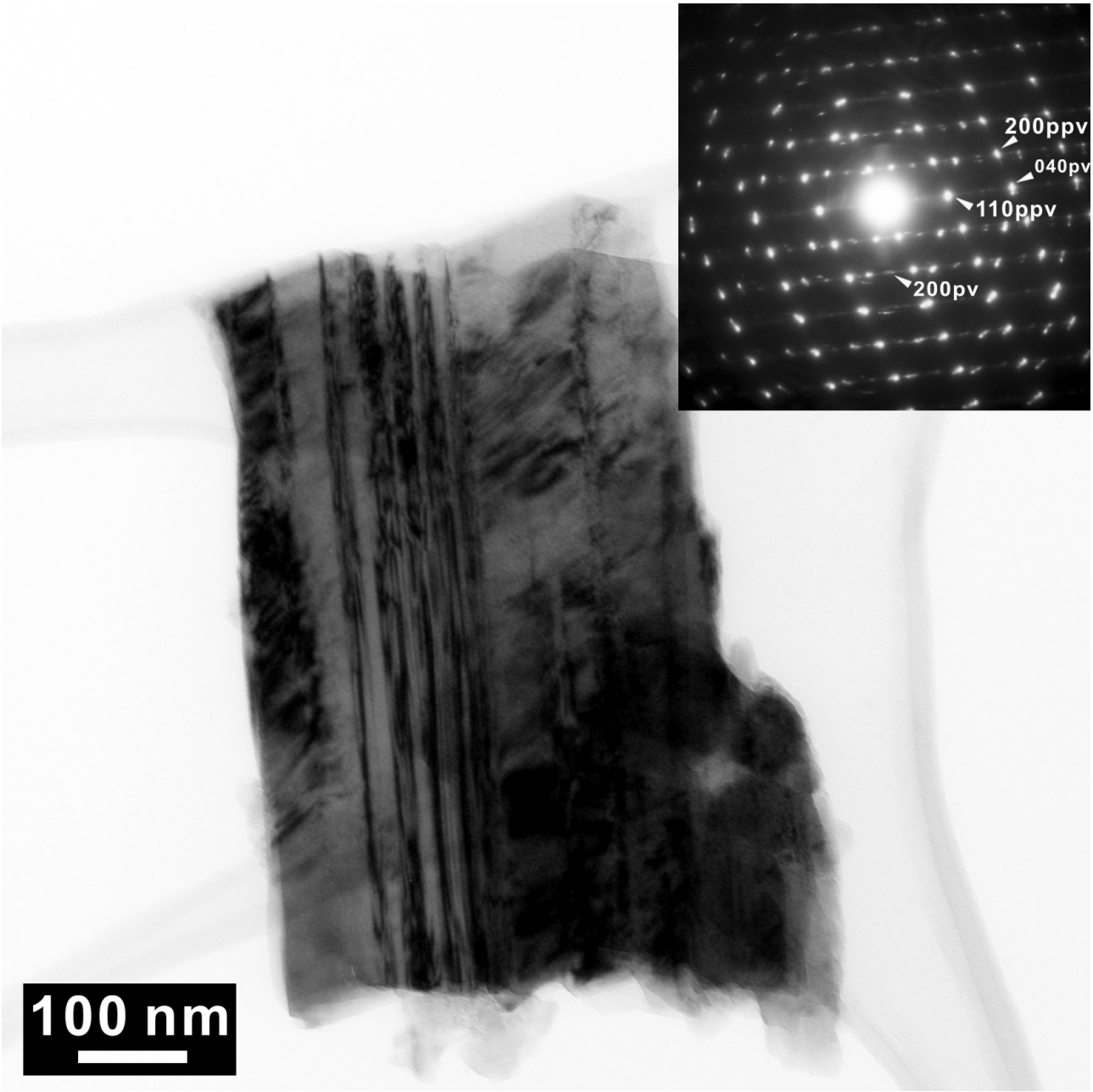

Figure S3. Bright-field TEM image of perovskite and post-perovskite domains. The inset is a selected area electron diffraction pattern along the [001]pv&ppv zone axis, which indicates a topotaxy between the perovskite and {110}ppv twin.

S4. Texture calculations.

Deformation driven texture development was simulated using the anisotropic visco-plastic self-consistent (VPSC) model (Molinari et al. 1987) as implemented by Lebensohn and Tomé (1993). This approach is designed to capture the interactions between crystals in a poly-crystalline solid undergoing macroscopic strain when the individual crystals deform by dislocation creep and interact with adjacent crystals. Full details of the approach and geophysically relevant examples can be found in (Kocks et al., 1998; Mainprice et al., 2008; Tommasi et al. 1999, 2000; Walker et al. 2011, Wenk et al. 2006, 2011). Here we only note that the key assumptions are that each crystal deforms only by strain on a set of specified slip systems exhibiting a visco-plastic rheological law, and that stress equilibrium and strain compatibility conditions implied by the inter-crystalline interactions are incorporated in an average way using a "1-site" homogenisation approximation. Single crystal slip system parameters used to simulate MgSiO3 perovskite and post-perovskite are listed in Table S1. We note that there is considerable controversy as to the most active slip systems in deforming post-perovskite and we therefore adopt three models intended to span the range of current uncertainty. We make use of the Tangent model (Lebensohn and Tomé, 1993) to parameterise the interactions between crystals.

Table S1: Slip system critical resolved stresses used for VPSC calculations. Each of the s slip systems yield following the visco-plastic law: $\dot{\gamma}^s = \dot{\gamma}_0 \left(\frac{\tau_r^s}{\tau_0^s}\right)^{n^s}$ where $\dot{\gamma}_0$ is a reference strain rate, τ_0^s is a reference shear stress, τ_r^s is the stress resolved on the slip system and n^s is a stress exponent (always taken as 3 in these calculations). No slip-system hardening law is imposed. The post-perovskite models are those used by Walker et al. (2011) with PPv P100 using the parameters of Merkel et al. (2007) favouring slip on the {011} and (100) planes. PPv P010 is taken from the Peierls-Nabarro modelling of Carrez et al. (2007a, 2007b) and Metsue et al. (2009) and with slip on the (010) dominating but with a rather isotropic yield surface. PPv P001 is intended to give slip on the (001) plane as observed by Miyagi et al. (2010). For perovskite (Pv) we

use parameters from the 100 GPa calculations of Mainprice et al. (2008). Activities of ∞ mean that this system cannot be activated for the particular parameter set.

Slip System	PPv P100	PPv P010	PPv P001	Pv
[100](001)	10	2.6	1	2.5
[010](001)	10	4.1	1	1.0
[001](010)	∞	1.0	∞	1.6
[001](100)	2	5.4	10	3.8
[010](100)	1	5.2	10	1.0
[001]{110}	4	2.9	10	1.9
<110>(001)	10	4.1	2	1.8
[100]{011}	∞	6.8	∞	∞
[100](010)	∞	4.7	∞	1.8
<110>{110}	1	8.8	10	2.0

We adopt a simple approach to simulate deformation in the lowermost mantle above the core mantle boundary and consider mantle deformation to be dominated by horizontal simple shear. Using the VPSC model we generated a description of lattice preferred orientation (LPO) for this deformation style. One difficulty with this approach is how the strength of the LPO is controlled. In a real material dislocation

motion is unlikely to be the only mechanism permitting deformation and the amount of dislocation motion is self limiting as dislocation multiplication and interactions between dislocations will tend to lead to slip-system hardening with increasing strain. This, in turn, introduces climb-limited deformation controlled by the motion of point defects. There is no experimental data on how quickly this process operates in lowermost mantle phases so, instead of introducing some arbitrary hardening law we accept that LPO will be generated unrealistically quickly as material is strained. A second control on the speed of texture development is the variation is hardness of different slip systems (the anisotropy of the single crystal yield surface). If many slip systems can accept strain with near equal values of their critical resolved shear stress crystals with different orientations will tend to slip on different slip system and thus not rotate in the same direction. On the other hand, if one particular slip system is much weaker than the others many of the crystals will tend to rotate to align this system to best accommodate the macroscopic strain, quickly giving a strong texture. The anisotropy of the single crystal yield surface is also not known for lowermost mantle phases. The net effect of these uncertainties is that the strength of the texture developed from the VPSC simulations will not be comparable to the strength of the true texture in the Earth. Several approaches have been taken in previous work to handle this difficulty including adding a large isotropic component to the calculated texture (Wenk et al, 2011), scaling magnitude of the applied strain (Merkel et al., 2007) or only considering the orientation of the resulting elastic anisotropy and not its magnitude (Nowacki et al., in review). Here, we reduce the magnitude of the applied strain to level that produces texture and seismic anisotropy of a reasonable strength and apply a total shear strain of $\gamma = 0.875$ to 500 post-perovskite crystals with an initially random distribution of orientations in thirty five steps.

Once the post-perovskite deformation texture has been generated we calculate the elastic and seismic anisotropy by forming the Voigt-Reuss-Hill average of the 500 rotated elastic stiffness tensors. This aggregate elasticity is used to calculate the velocities of the seismic P- and S-waves and thus the seismic anisotropy. These calculations are performed using the MSAT software (Walker and Wookey, 2012). In

order to compare with models of global seismic anisotropy which impose vertically transverse isotropy (VTI) on the data we calculate the velocity of vertically (V_{SV}) and horizontally (V_{SH}) polarised S-waves propagating parallel to the core mantle boundary (CMB) and the velocity of P-waves propagating normal to (V_{PV}) and parallel to (V_{PH}) the CMB in a medium on which VTI has been imposed. We impose this symmetry by forming the Voigt-Reuss-Hill average elasticity of many replicas of our calculated tensor rotated around the vertical axis. We then extract the $\xi = V_{SH}^2/V_{SV}^2$ and $\phi = V_{PV}^2/V_{PH}^2$ parameters usually reported in studies of global seismic anisotropy. These are reported in Table S2.

Table S2: Parameters describing the anisotropy of the textures shown in Figure 2 of the main text after imposing VTI on the generally anisotropic results. Zero is isotropic.

Stage of simulation (see Figure 2)	ln(ξ)	ln(ϕ)
(a)	7.45%	1.01%
(b)	-4.24%	1.42%
(c)	-0.16%	-4.69%

To evaluate the anisotropy after the post-perovskite to perovskite phase transition (b in Table S2), and simulate the effect of heating the mantle as it moves across the core mantle boundary, we took the texture of the strain post-perovskite, rotated each crystal according to the experimentally determined orientation relationship between the two phases and then evaluated the seismic anisotropy assuming 100%

conversation from post-perovskite to perovskite. In order to do this we first formed unit vectors along the principal axes of the post-perovskite crystal, and in the directions expected for the perovskite crystal (randomly and uniformly choosing between cases where [010]pv || [110]ppv and [010]pv || [1-10]ppv to account for the post-perovskite twinning). These vectors are then used to build a rotation matrix to describe the effect of the phase transition on each crystal. The code used for this process forms a new usage example for the MSAT toolkit and will be available for download as part of the next minor revision (version 1.0.1 – see http://www1.gly.bris.ac.uk/MSAT/).

In order to further determine how long the transformed texture can persist in the lower mantle undergoing further deformation we performed additional VPSC calculations on perovskite aggregates starting from the calculated transformed texture (c in Table S2). While the texture and seismic anisotropy does change this change is not as profound as the difference between post-perovskite and perovskite and maintains the same basic signature of fast vertically polarised shear waves and slow horizontally polarised shear waves.

Carrez, P., D. Ferré, and P. Cordier (2007a), Implications for plastic flow in the deep mantle from modelling dislocations in $MgSiO_3$ minerals, Nature, 446, 68–70, doi:10.1038/nature05593.

Carrez, P., D. Ferré, and P. Cordier (2007b), Peierls-Nabarro model for dislocations in $MgSiO_3$ post-perovskite calculated at 120 GPa from first principles, Philos. Mag., 87, 3229–3247, doi:10.1080/14786430701268914.

Lebensohn, R. A., and C. N. Tomé (1993), A self-consistent anisotropic approach for the simulation of plastic deformation and texture development of polycrystals: Application to zirconium alloys, Acta Metall. Mater., 41(9), 2611–2624, doi:10.1016/0956-7151(93)90130-K.

Mainprice et al. (2008), EPSL 271:135-144.

Merkel, S., A. K. McNamara, A. Kubo, S. Speziale, L. Miyagi, Y. Meng, T. S. Duffy, and H.-R. Wenk (2007), Deformation of (Mg,Fe)SiO_3 post-perovskite and D″ anisotropy, Science, 316, 1729–1732, doi:10.1126/science.1140609.

Metsue, A., P. Carrez, D. Mainprice, and P. Cordier (2009), Numerical modelling of dislocations and deformation mechanisms in $CaIrO_3$ and $MgGeO_3$ post-perovskites — Comparison with $MgSiO_3$ post-perovskite, Phys. Earth Planet. Inter., 174, 165–173, doi:10.1016/j.pepi.2008.04.003

Miyagi, L., W. Kanitpanyacharoen, P. Kaercher, K. K. M. Lee, and H.-R. Wenk (2010), Slip systems in $MgSiO_3$ post-perovskite: implications for D″ anisotropy, Science, 329, 1636–1638.Molinari, A., G. Canova and S. Ahzi Acre Metall., 35 (1987) 2983.

Nowacki, A., A. M. Walker, J. Wookey, and J.-M. Kendall (in review) Submitted to Geophysical Journal International.

Kocks, U. F., C. N. Tomé, and H.-R. Wenk (1998) Texture and Anisotropy. Preferred Orientations in Polycrystals and Their Effect on Materials Properties, Cambridge Univ. Press, Cambridge, U. K.

Tommasi, A., A. B. Tikoff, and A. Vauchez (1999), Upper mantle tectonics: three-dimensional deformation, olivine crystallographic fabrics and seismic properties, Earth Planet. Sci. Lett., 168(1–2), 173–186, doi:10.1016/S0012-821X(99)00046-1.

Tommasi, A., D. Mainprice, G. Canova, and Y. Chastel (2000), Viscoplastic self-consistent and equilibrium-based modelling of olivine lattice preferred orientations: Implications for the upper mantle seismic anisotropy, J. Geophys. Res., 105, 7893–7980.

Walker, A. M. and J. Wookey (2012) "MSAT - A new toolkit for the analysis of elastic and seismic anisotropy" Computers and Geosciences, 49, pp.81-90. doi:10.1016/j.cageo.2012.05.031

Walker, A. M., A. M. Forte, J. Wookey, A. Nowacki and J.-M. Kendall (2011) "Elastic anisotropy of D″ predicted from global models of mantle flow" Geochemistry, Geophysics, Geosystems, 12, art.no. Q10006. doi:10.1029/2011GC003732

Wenk, H.-R., S. Speziale, A. K. McNamara, and E. J. Garnero (2006), Modeling lower mantle anisotropy development in a subducting slab, Earth Planet. Sci. Lett., 245, 302–314.

Wenk, H.-R., S. Cottaar, C. N. Tomé, A. McNamara, and B. Romanowicz (2011), Deformation in the lowermost mantle: From polycrystal plasticity to seismic anisotropy, Earth Planet. Sci. Lett., 306, 33–45, doi:10.1016/j.epsl.2011.03.021.